

2021-11

Uncertainty quantification in shallow water-sediment flows: A stochastic Galerkin shallow water hydro-sediment-morphodynamic model

Li, J

<http://hdl.handle.net/10026.1/17640>

10.1016/j.apm.2021.06.031

Applied Mathematical Modelling

Elsevier BV

All content in PEARL is protected by copyright law. Author manuscripts are made available in accordance with publisher policies. Please cite only the published version using the details provided on the item record or document. In the absence of an open licence (e.g. Creative Commons), permissions for further reuse of content should be sought from the publisher or author.

Uncertainty quantification in shallow water-sediment flows: A Stochastic Galerkin Shallow water Hydro-Sediment-Morphodynamic Model

Ji Li^{a, b}, Zhixian Cao^{a *}, Alistair G. L. Borthwick^{c, d}

^a *State Key Laboratory of Water Resources and Hydropower Engineering Science, Wuhan University, Wuhan 430072, China;*

^b *Zienkiewicz Centre for Computational Engineering, [Faculty of Science and Engineering](#), Swansea University, Swansea SA1 8EN, UK;*

^c *Institute for Infrastructure and Environment, The University of Edinburgh, Edinburgh EH9 3FG, UK.*

^d *School of Engineering, Computing and Mathematics, University of Plymouth, Plymouth PL4 8AA, UK.*

*Corresponding authors: Zhixian Cao, e-mail: zxcao@whu.edu.cn

Highlights

- A stochastic shallow water hydro-sediment-morphodynamic model is proposed
- A well-balanced, operator-splitting-based, stochastic Galerkin method is used
- The model satisfactorily reproduces typical flow-sediment-bed evolution with uncertainty

Declarations of interest: none

Abstract

All shallow water hydro-sediment-morphodynamic (SHSM) models are prone to uncertainty arising from inadequate representation of the underlying physics and error in input parameters. At the time of writing, most SHSM models solve deterministic problems, whilst studies of uncertainty quantification in SHSM models remain rare. Here a new stochastic SHSM model is proposed, extended from a well-balanced, operator-splitting-based, generalized polynomial chaos stochastic Galerkin (gPC-SG) solver of the one-dimensional shallow water hydrodynamic equations. A series of probabilistic numerical tests are carried out, corresponding to idealized test of dam break flow over a fixed bed and laboratory experiments of flow-sediment-bed evolutions induced by a sudden dam break and by landslide dam failure. The proposed modelling framework shows promise for uncertainty quantification of shallow water-sediment flows over erodible beds.

Keywords: uncertainty quantification; shallow water hydro-sediment-morphodynamic model; operator-splitting; generalized polynomial chaos; stochastic Galerkin method

1. Introduction

Shallow free surface water-sediment flows are key drivers of mass transport and morphological evolution on Earth. Surface hydro-sediment-morphodynamics processes include general fluvial sediment-laden flows and geophysical mass flows such as debris flows, landslides, and turbidity currents. Mathematical modelling has become one of the most proactive approaches to enhancing our understanding of shallow water-sediment flows over the past half-century [1]. Whereas fully three-dimensional models may facilitate very detailed resolution of such processes [2-4], such models incur excessively high computing overheads and thus may not be practicable for large-scale prototype engineering applications. Instead, shallow water hydro-sediment-morphodynamic (SHSM) models have witnessed significant developments over the last two decades, featuring a sensible balance between theoretical integrity and practical applicability, including depth-averaged quasi single-phase and two-phase models (e.g., [5-13]) as well as double layer-averaged quasi single-phase and two-phase models (e.g., [14-19]). Unlike traditional shallow water hydrodynamic equations for clear water flows [20], the SHSM equations explicitly accommodate interactions between flow, sediment transport, and bed evolution.

In principle, SHSM model equations are a system of nonlinear hyperbolic equations built upon fundamental mass and momentum conservation laws. Inevitably, SHSM models propagate uncertainty arising from incomplete knowledge of the underlying physics and error in physical input parameters. For example, parameter uncertainty can enter the system via initial and boundary conditions, such as measurement errors in topography and inflow discharge, choice of friction coefficient, selection of empirical parameters used in sediment

1 transport estimation. Although many SHSM model studies have been undertaken (e.g.,
2
3 [5-19]), they almost exclusively concern deterministic problems. Even though existing SHSM
4
5 models are able to achieve quantitative matches between predictions and observations, their
6
7 developments and applications hinge upon the user's ability to assign accurate numerical
8
9 values to various parameters in the governing equations. To fully understand the computed
10
11 results and subsequently the underlying physics, it is therefore imperative to incorporate
12
13 uncertainty from the onset of the simulations and not as an afterthought [21]. However, to
14
15 date, there has been a lack of studies on uncertainty quantification of SHSM equations.
16
17
18
19
20
21
22

23 Uncertainty quantification (UQ) is not new in the broad field of partial differential
24
25 equations (PDEs). Substantial effort has been devoted to applying polynomial chaos or
26
27 generalized polynomial chaos (gPC) expansions as basis functions to represent random space
28
29 [22-24]. They offer good alternatives to statistical methods for uncertainty quantification such
30
31 as Monte-Carlo simulations and their variants, by substantially reducing or eliminating the
32
33 need for repetitive sampling [21]. Non-intrusive polynomial chaos methods repeatedly
34
35 sample a deterministic model with different input values, and then use the numerical outputs
36
37 to construct a stochastic solution based on interpolation and quadrature rules [23, 25].
38
39 Intrusive methods make a Galerkin projection in stochastic space to produce a system of
40
41 deterministic equations, which are solved in a single model run to obtain the stochastic
42
43 moments of the solution of the original uncertain problem. In a comparison of intrusive and
44
45 non-intrusive approaches for the diffusion equation with random inputs [26], it has been
46
47 found that the intrusive stochastic Galerkin method incurred a lower computational cost.
48
49 Furthermore, the stochastic Galerkin method has inherent theoretical advantages due to its
50
51
52
53
54
55
56
57
58
59
60
61
62
63
64
65

basis in a Galerkin framework.

Existing generalized polynomial chaos stochastic Galerkin (gPC-SG) methods have been successfully applied to many physical and engineering problems, including diffusion [27], gas dynamics [28, 29], disperse two-phase flow [30], and shallow water hydrodynamics [31, 32], where spectral convergence was obtained when the underlying solution was sufficiently smooth. However, application of the gPC-SG approach to nonlinear hyperbolic systems of conservation laws faces the major challenge of loss of global hyperbolicity [33]. For linear hyperbolic systems and scalar hyperbolic conservation laws, the gPC-SG approximation yields a system of gPC coefficients that is always hyperbolic; thus gPC-SG methods are available for uncertainty quantification of such equations [24]. Also, if the original system is symmetric, such as the Hamilton-Jacobi equation [34], the gPC-SG approximation remains hyperbolic. However, when gPC-SG methods are applied to general nonlinear (non-symmetric) hyperbolic systems, the resulting system of gPC coefficients is not necessarily globally hyperbolic because its Jacobian matrices may generate complex eigenvalues. This phenomenon is somewhat similar to hyperbolicity loss in Grad's thirteen-moment closure of the Boltzmann equation [35]. Consequently, extra effort is required to ensure system remain well-behaved. One approach is to use gPC approximations for entropic variables [36]. Specifically, in bijection with conservative variables, the new entropic variables are introduced by solving a minimization problem at every mesh point and time step; however, this would be computationally expensive for large-scale problems. Another alternative approach is to use Roe variables [37], but this is restricted to systems that admit Roe linearization. Moreover, switching is required between the Roe and original

variables at every grid point and time step, which involves solving nonlinear algebraic equations using a trust-region-dogleg algorithm.

Recently, an operator-splitting stochastic Galerkin method was proposed for the Euler equations for gas dynamics subject to uncertainty [38], and a well-balanced version developed for the shallow water hydrodynamic equations without bed friction [39]. The main idea behind this method is to split the underlying hyperbolic system into a linear hyperbolic system and linear or nonlinear scalar equations with variable coefficients and source terms, for which the gPC-SG method obtains globally hyperbolic discretization. Subsequently, the gPC-SG method is applied to each of the subproblems, resulting in a hyperbolic system of gPC coefficients. In the gPC-SG method, the underlying system is solved in terms of orthogonal polynomial series [24, 40], whose coefficients satisfy deterministic systems of time-dependent PDEs. Given that the gPC-SG system of equations for the coefficients is guaranteed hyperbolic, it can be numerically solved by a finite-volume Godunov-type shock-capturing method that is capable of capturing subcritical, supercritical, and transcritical flows.

This paper presents a well-balanced, operator-splitting, stochastic Galerkin model of the one-dimensional (1D) shallow water hydro-sediment-morphodynamic equations with uncertainty. The model extends the solver devised by Chertock et al. [39] for frictionless clear water flow to frictional shallow water-sediment flow over an erodible bed. Unlike Chertock et al. [39] who employed a well-balanced second-order semi-discrete central-upwind scheme, we use a stochastic reformulation of a well-balanced scheme that utilises a surface gradient method (SGM) version of the finite volume Slope Limiter Centred (SLIC) scheme.

Probabilistic benchmark tests verify the resulting stochastic model for wave propagation triggered by idealized dam break over a fixed bed [39] and flow-sediment-bed evolutions driven by a sudden dam break [14] and by landslide dam failure [41].

To the authors' knowledge, this is the first attempt towards modelling probabilistic shallow water-sediment flows over an erodible bed in a stochastic Galerkin setting. The present study does not aim to address numerical difficulties in handling discontinuities in random space using the gPC approximation, which may trigger the Gibbs phenomenon. In fact, such challenges can be addressed by [machine learning to track discontinuities \[42\]](#), [adaptive level set methods for discontinuity detection \[43\]](#), and [adaptive minimum spanning tree multielement methods combined with vector machines for discontinuity identification \[44\]](#).

2. Deterministic SHSM model

2.1. Governing equations

Consider longitudinal one-dimensional shallow water-sediment flow over an erodible bed composed of uniform, non-cohesive sediment of particle diameter d_s . The governing shallow water hydro-sediment-morphodynamic equations can be derived by directly applying the Reynolds transport theorem in fluid dynamics [45], and include mass and momentum conservation equations for the water-sediment mixture and separate mass conservation equations for sediment and bed material. The resulting system of equations can be expressed in standard, well-structured conservation form as follows [6]:

$$\frac{\partial \mathbf{U}}{\partial t} + \frac{\partial \mathbf{F}(\mathbf{U})}{\partial x} = \mathbf{S}_b + \mathbf{S}_f \quad (1)$$

in which

$$\mathbf{U} = \begin{bmatrix} \eta \\ hu \\ hc \end{bmatrix}, \quad \mathbf{F} = \begin{bmatrix} q \\ hu^2 + 0.5g(\eta^2 - 2\eta z_b) \\ huc \end{bmatrix} \quad (2a, b)$$

$$\mathbf{S}_b = \begin{bmatrix} 0 \\ -g\eta \frac{\partial z_b}{\partial x} \\ 0 \end{bmatrix}, \quad \mathbf{S}_f = \begin{bmatrix} 0 \\ N(\mathbf{U}) \\ E - D \end{bmatrix} \quad (2c, d)$$

$$N(\mathbf{U}) = -\frac{\tau_b}{\rho} - \frac{(\rho_s - \rho_f)gh^2}{2\rho} \frac{\partial c}{\partial x} - \frac{(\rho_0 - \rho)(E - D)u}{(1 - p)\rho} \quad (2e)$$

and

$$\frac{\partial z_b}{\partial t} = -\frac{E - D}{1 - p} \quad (3)$$

where \mathbf{U} represents the vector of conservative dependent variables; \mathbf{F} is the vector of flux variables; \mathbf{S}_b is the vector of bed gradient terms; \mathbf{S}_f is the vector of other terms including friction and effects from mass exchange with the bed; t is time, x is streamwise coordinate; g is gravitational acceleration; h is the depth of the water-sediment mixture, z_b is the bed elevation, $\eta = h + z_b$ is the free-surface elevation above the bed; u is the depth-averaged velocity of the water-sediment mixture in the streamwise (x -) direction; c is the depth-averaged volumetric sediment concentration; ρ_f and ρ_s are the pure densities of the water and sediment phases; $\rho = \rho_s c + \rho_f(1 - c)$ is the density of the water-sediment mixture; $\rho_0 = \rho_s(1 - p) + \rho_f p$ is the density of the bed material; p is the bed sediment porosity, and thus $1 - p$ is the volumetric sediment concentration of the stationary bed; τ_b is the bottom shear stress for the water-sediment mixture; and E and D are the

size-specific sediment entrainment and deposition fluxes.

2.2. Model closures

To close the governing equations, relationships must be introduced to determine shear stresses and sediment exchange fluxes.

In general, the boundary resistances of unsteady and non-uniform flows are substantially different from those of steady and uniform flows. When sediment transport is also involved, boundary resistance alters as the flow geometry evolves dynamically. However, to date, there are no generally applicable relationships available to represent boundary resistances for shallow water-sediment flows. Empiricism and uncertainty in estimation of bed shear stress are common to all models of shallow water-sediment flows. Here, we use the Manning resistance relationship originally developed for steady, uniform flow to determine the bed shear stress from

$$\tau_b = \rho g h \frac{n^2 u^2}{h^{4/3}} \quad (4)$$

where n is the Manning roughness parameter.

Two distinct primary mechanisms promote sediment exchange between the flow and the bed: bed sediment entrainment due to turbulence; and sediment deposition by gravitational action. Sediment particle-particle interactions may also modify such exchange processes. Although computational models of sediment transport and morphological evolution depend on accurate determination of entrainment and deposition fluxes, current formulations hinge

upon a series of premises. Here, we follow the conventional practice in fluvial hydraulics [1], and estimate the deposition flux from the local near-bed sediment concentration and settling velocity. To specify the entrainment fluxes, we follow a widely used approach that assumes entrainment occurs at the same rate as in the capacity regime, whereby the entrainment flux is equal to the deposition flux, and computed from the near-bed sediment concentration at capacity and settling velocity. Accordingly, the entrainment and deposition fluxes are estimated from

$$E = \alpha \omega c_e \quad \text{and} \quad D = \alpha \omega c \quad (5a, b)$$

where ω is the settling velocity of the particle grain calculated using Zhang's formula [46],

$$\omega = \sqrt{(13.95 \frac{\nu_{\mu f}}{d_s})^2 + 1.09 s g d_s} - 13.95 \frac{\nu_{\mu f}}{d_s} \quad (6)$$

where $\nu_{\mu f}$ is the kinematic viscosity of the fluid phase; s is the specific gravity of sediment $= (\rho_s - \rho_f) / \rho_f$; α is an empirical parameter representing the difference between near-bed sediment concentration c_b and depth-averaged sediment concentration c .

Here, α is a unified constant estimated by calibration tests during model set up [8].

Sediment concentration c_e at capacity is

$$c_e = q_b / (h u) \quad (7a)$$

where q_b is the transport rate at capacity regime, which is calculated by the Wu formula [1]

as follows

$$\frac{q_b}{\phi \sqrt{s g d_s^3}} = 0.0053 \left[\left(\frac{n'}{n} \right)^{1.5} \frac{\tau_b}{\tau_c} - 1 \right]^{2.2} + 0.0000262 \left[\left(\frac{\tau}{\tau_c} - 1 \right) \frac{u}{\omega} \right]^{1.74} \quad (7b)$$

where ϕ is a modification coefficient; $n' = d_{s,50}^{1/6} / 20$ is the Manning roughness

corresponding to grain resistance; τ is shear stress imposed by channel cross-section bed and walls; τ_c is the critical shear stress for incipient motion of bed material, approximated by $\tau_c = 0.03(\rho_s - \rho_f)gd_s$. Eq. (5a) is applicable when there is sufficient sediment supply from the bed. Otherwise, the sediment entrainment flux vanishes where the bed comprises rigid material (e.g., steel or concrete) and is locally non-erodible.

2.3. A splitting operator

As bed deformation is entirely determined by local entrainment and deposition fluxes under the non-capacity framework for sediment transport, Eq. (3) is separated from the remaining equations and can be readily solved. Following Chertock et al. [39], we split the governing equation system (1) into the following two subsystems

$$\frac{\partial \mathbf{U}}{\partial t} + \frac{\partial \mathbf{F}^I(\mathbf{U})}{\partial x} = 0 \quad (8a)$$

and

$$\frac{\partial \mathbf{U}}{\partial t} + \frac{\partial \mathbf{F}^{II}(\mathbf{U})}{\partial x} = \mathbf{S}_b + \mathbf{S}_f \quad (8b)$$

in which

$$\mathbf{U} = \begin{bmatrix} \eta \\ q \\ h_s \end{bmatrix}, \quad \mathbf{F}^I = \begin{bmatrix} q \\ a^2 \eta \\ q_s \end{bmatrix}, \quad \mathbf{F}^{II} = \begin{bmatrix} 0 \\ \psi + 0.5g(\eta^2 - 2\eta z_b) - a^2 \eta \\ 0 \end{bmatrix} \quad (8c, 8d, e)$$

where $q = hu$ is the discharge; $h_s = hc$ is the equivalent thickness of the sediment phase;

$q_s = h_s u$ is the sediment discharge; $\psi = hu^2 = q^2/h$.

Assuming $\mathbf{U}(x, t)$ is available at time t , let \mathbf{S}_I and \mathbf{S}_{II} denote the solution operators for the subsystem (8a) and (8b), respectively. Then, an approximate solution at the next time level $t + \Delta t$ can be obtained by using the following operator splitting method:

$$\mathbf{U}(x, t + \Delta t) \approx \mathbf{S}_I(\Delta t) \mathbf{S}_{II}(\Delta t) \mathbf{U}(x, t) \quad (9)$$

For a practical implementation, one needs to choose a proper splitting time step Δt and replace the solution operators, \mathbf{S}_I and \mathbf{S}_{II} in Eq. (9) with their finite volume discretizations, which will be described in detail in Section 2.4.

The first subsystem (8a) is a linear hyperbolic system whose Jacobian has three distinct real eigenvalues $\lambda_{1,2} = \pm a$ and $\lambda_3 = u$, where the parameter $a > 0$ is chosen to satisfy the following sub-characteristic condition:

$$-a \leq u - \sqrt{gh} \leq u + \sqrt{gh} \leq a \quad (10)$$

The second system (8b) is essentially a scalar Burgers equation for q with variable coefficient and source term, given that η and h_s remain constant in time in Eq. (8b). Furthermore, the value of a is set larger than the characteristic speed related to the second equation of the second subsystem (8b), such that

$$a = \sup \left\{ \max(|u| + \sqrt{gh}, 2|u|) \right\} \quad (11)$$

It is straightforward to check that under the sub-characteristic condition (10), each subsystem is strictly hyperbolic. Therefore, after applying the gPC-SG approximation, each subsystem is globally hyperbolic for the gPC coefficients.

2.4. Numerical algorithm

A well-balanced numerical algorithm presented in Qian et al. [8] is adapted to solve system Eq. (8). Briefly, within the framework of finite volume SLIC scheme [20], a SGM is incorporated to achieve a well-balanced solution to the governing equations. Applying an explicit finite volume discretization [20] along with a second-order Runge-Kutta (RK) method for the source term \mathbf{S}_f , one has

$$\mathbf{U}_i^* = \mathbf{U}_i^n - \frac{\Delta t}{\Delta x} [\mathbf{F}_{i+1/2}^I - \mathbf{F}_{i-1/2}^I] \quad (12a)$$

$$\mathbf{U}_i^\dagger = \mathbf{U}_i^* - \frac{\Delta t}{\Delta x} [\mathbf{F}_{i+1/2}^{II} - \mathbf{F}_{i-1/2}^{II}] + \Delta t \bar{\mathbf{S}}_{b,i} \quad (12b)$$

and

$$\mathbf{U}_i^{n+1} = \mathbf{U}_i^\dagger + \Delta t \mathbf{S}_f^{RK} \quad (12c)$$

where Δt is the time step; Δx is the spatial step; subscript i denotes the spatial node index; superscript n denotes the time step index; superscript $*$ indicates the state after calculating the variables from Eq. (12a), superscript \dagger denotes the state after Eq. (12b); and $\mathbf{F}_{i+1/2}^{Ior II}$ and $\mathbf{F}_{i-1/2}^{Ior II}$ represent the inter-cell numerical fluxes.

The bed slope source term $\bar{\mathbf{S}}_{bi}$ is discretized with a centered difference scheme [8] because it is well-balanced with the flux gradients.

$$\bar{\mathbf{S}}_{bi} = \begin{pmatrix} 0 \\ -g \frac{\bar{\eta}_{i+1/2}^L + \bar{\eta}_{i-1/2}^R}{2} \frac{z_{b,i+1/2} - z_{b,i-1/2}}{\Delta x} \\ 0 \end{pmatrix} \quad (13)$$

where $\bar{\eta}_{i+1/2}^L$ and $\bar{\eta}_{i-1/2}^R$ are the evolved variables obtained from Step 2 in the following flux computation. The source term \mathbf{S}_f is determined using the second-order Runge-Kutta method as follows

$$\mathbf{S}_f^{RK} = [\mathbf{S}_f(\mathbf{U}_i^{\dagger 1}) + \mathbf{S}_f(\mathbf{U}_i^{\dagger 2})]/2 \quad (14)$$

in which $\mathbf{U}_i^{\dagger 1} = \mathbf{U}_i^\dagger$, $\mathbf{U}_i^{\dagger 2} = \mathbf{U}_i^{\dagger 1} + \Delta t \mathbf{S}_f(\mathbf{U}_i^{\dagger 1})$

The bed deformation is updated by the discretization of Eq. (3)

$$z_{b,i}^{n+1} = z_{b,i}^n - \Delta t \left(\frac{E - D}{1 - p} \right)_i^{RK} \quad (15)$$

where the superscript RK indicates that the sediment exchange is estimated using the second-order Runge-Kutta method for the source terms.

The numerical fluxes $\mathbf{F}_{i+1/2}^{Ior \Pi}$ and $\mathbf{F}_{i-1/2}^{Ior \Pi}$ involved in Eqs. (12a and 12b) are evaluated in the following three steps using the well-balanced SGM version of the finite volume SLIC scheme.

Step 1: Data reconstruction of inter-cell variables $\mathbf{U}_{i+1/2}^L$ and $\mathbf{U}_{i+1/2}^R$ to achieve second-order accuracy in space

$$\mathbf{U}_{i+1/2}^L = \mathbf{U}_i^n + \frac{1}{2} \boldsymbol{\phi}_{i-1/2} (\mathbf{U}_i^n - \mathbf{U}_{i-1}^n) \quad (16a)$$

$$\mathbf{U}_{i+1/2}^R = \mathbf{U}_{i+1}^n + \frac{1}{2} \boldsymbol{\phi}_{i+1/2} (\mathbf{U}_{i+1}^n - \mathbf{U}_i^n) \quad (16b)$$

where the superscripts L and R represent the left and right sides of the cell interfaces; and the vector $\boldsymbol{\phi}$ is a slope limiter. Here, the MinBee limiter is chosen for the limiter function $\boldsymbol{\phi}$, as described by Toro [5]. Besides, the evaluation of inter-cell water depths are obtained from the reconstructed water levels

$$h_{i+1/2}^L = \eta_{i+1/2}^L - z_{b,i+1/2}^L, \quad h_{i+1/2}^R = \eta_{i+1/2}^R - z_{b,i+1/2}^R \quad (17a, b)$$

where the inter-cell bed elevations are approximated by linear interpolation

$$z_{b,i+1/2}^L = z_{b,i+1/2}^R = (z_{b,i} + z_{b,i+1})/2 \quad (18)$$

Step 2: Evolution of inter-cell variables over a time step of $\Delta t/2$ to achieve second-order accuracy in time. To satisfy the well-balanced property when the SGM is adopted, the contribution due to gravity must be included:

$$\mathbf{U}_{i+1/2}^{*L} = \mathbf{U}_{i+1/2}^L - \frac{\Delta t}{2\Delta x} [\mathbf{F}^I(\mathbf{U}_{i+1/2}^L) - \mathbf{F}^I(\mathbf{U}_{i-1/2}^R)] \quad (19a)$$

$$\mathbf{U}_{i+1/2}^{*R} = \mathbf{U}_{i+1/2}^R - \frac{\Delta t}{2\Delta x} [\mathbf{F}^I(\mathbf{U}_{i+3/2}^L) - \mathbf{F}^I(\mathbf{U}_{i+1/2}^R)] \quad (19b)$$

$$\bar{\mathbf{U}}_{i+1/2}^L = \mathbf{U}_{i+1/2}^{*L} - \frac{\Delta t}{2\Delta x} [\mathbf{F}^{II}(\mathbf{U}_{i+1/2}^{*L}) - \mathbf{F}^{II}(\mathbf{U}_{i-1/2}^{*R})] + \frac{\Delta t}{2} \mathbf{S}_{b,i} \quad (19c)$$

$$\bar{\mathbf{U}}_{i+1/2}^R = \mathbf{U}_{i+1/2}^{*R} - \frac{\Delta t}{2\Delta x} [\mathbf{F}^{II}(\mathbf{U}_{i+3/2}^{*L}) - \mathbf{F}^{II}(\mathbf{U}_{i+1/2}^{*R})] + \frac{\Delta t}{2} \mathbf{S}_{b,i+1} \quad (19d)$$

where $\mathbf{S}_{b,i}$ is discretized with the centred difference scheme (Eq. 13) as a function of the reconstructed variables $\eta_{i+1/2}^{*L}$ and $\eta_{i-1/2}^{*R}$. Similarly, the evolving water depths in this step are given by

$$\bar{h}_{i+1/2}^L = \bar{\eta}_{i+1/2}^L - z_{b,i+1/2}^L, \quad \bar{h}_{i+1/2}^R = \bar{\eta}_{i+1/2}^R - z_{b,i+1/2}^R \quad (20a, b)$$

Step 3: Evaluation of numerical fluxes. The numerical inter-cell fluxes $\mathbf{F}_{i+1/2}^{Ior II}$ are evaluated according to the First ORder CEntred (FORCE) method [20] with the evolved inter-cell variables $\bar{\mathbf{U}}_{i+1/2}^L$ and $\bar{\mathbf{U}}_{i+1/2}^R$.

$$\mathbf{F}_{i+1/2} = \frac{1}{2} (\mathbf{F}_{i+1/2}^{LF} + \mathbf{F}_{i+1/2}^{LW}) \quad (21a)$$

$$\mathbf{F}_{i+1/2}^{LF} = \frac{1}{2} [\mathbf{F}(\bar{\mathbf{U}}_{i+1/2}^L) + \mathbf{F}(\bar{\mathbf{U}}_{i+1/2}^R)] + \frac{1}{2} \frac{\Delta x}{\Delta t} (\bar{\mathbf{U}}_{i+1/2}^L - \bar{\mathbf{U}}_{i+1/2}^R) \quad (21b)$$

$$\mathbf{F}_{i+1/2}^{LW} = \mathbf{F}(\mathbf{U}_{i+1/2}^{LW}) \quad (21c)$$

$$\mathbf{U}_{i+1/2}^{LW} = \frac{1}{2}(\bar{\mathbf{U}}_{i+1/2}^L + \bar{\mathbf{U}}_{i+1/2}^R) + \frac{1}{2} \frac{\Delta t}{\Delta x} [\mathbf{F}(\bar{\mathbf{U}}_{i+1/2}^L) - \mathbf{F}(\bar{\mathbf{U}}_{i+1/2}^R)] \quad (21d)$$

To satisfy the well-balanced property, a special treatment is performed at wet-dry interfaces. If the water surface in a wet cell is lower than the bed elevation of its adjacent dry cell, then the bed elevation and water level of this dry cell are both set at the level of the water surface of the wet cell temporarily during the flux calculation operation. For example, if the cell i is wet while the adjacent cell $i+1$ is dry and $\eta_i < \eta_{i+1}$ then $\eta_i = z_{b,i+1} = \eta_{i+1}$, and the depth in the cell $i+1$ remains zero as a consequence. The occurrence of very small water depth in a numerical simulation can lead to instability due to the estimated bed resistance approaching infinity, especially at wet-dry interfaces. To avoid this difficulty, any computed water depth lower than a threshold value is set to be zero. Considering a motionless steady state problem ($\eta = \eta_0$ and $q = 0$), it is straightforward to prove the well-balanced property of the above numerical algorithm (c.f. Qian et al. [8]).

3. Stochastic SHSM model

3.1. gPC-SG Method

The gPC expansion introduces a new dimension to the physical problem in order to account for uncertainty. Variables in the governing differential equations are represented by a series of orthogonal polynomials, each of which, for computational purposes, is truncated after a finite number of modes. In the present study, the vector of conserved variables in the nonlinear SHSM equations is expanded as follows

$$\mathbf{U}(x, t, \xi) = \sum_{k=0}^{M-1} \hat{\mathbf{U}}_k(x, t) \Phi_k(\xi), \quad M = \binom{d+N}{d} \quad (22)$$

where $\hat{\mathbf{U}}_k(x, t)$ are gPC coefficients; $\xi = (\xi_1, \dots, \xi_d) \in \mathbb{R}^d$, $d \geq 1$ is a random vector with independent and identically distributed components; $\Phi_k(\xi)$ are d -variate orthonormal polynomials of total degree up to $N \geq 1$ from \mathbb{P}_N^d satisfying

$$\int \Phi_k(\xi) \Phi_l(\xi) \mu(\xi) d\xi = \delta_{kl}, \quad 0 \leq k, l \leq M-1 \quad (23)$$

Here $\mu(\xi)$ is the probability density function of ξ , and δ_{kl} is the Kronecker symbol. The choice of orthogonal polynomials depends on the distribution function of ξ . For example, a Gaussian distribution defines Hermite polynomials, whereas a uniform distribution defines Legendre polynomials, etc. In particular, when multiple sources of uncertainty are considered, i.e., $d > 1$, the probability distributions become multivariate and $\Phi(\xi)$ are multidimensional polynomials of degree up to N of ξ . A graded lexicographic ordering scheme for multiple indexes [27] is therefore used to reorder the polynomials into a spatial single index. Note that as such dimensionality increases, the number of basis functions can quickly grow, exponentially increasing computational and storage costs so that they spiral out of control – the so-called “curse-of-dimensionality” [27]. For simplicity, the present study is limited to one-dimensional random uncertainty (i.e., $d = 1$).

3.2. Stochastic Galerkin reformulation of the deterministic model

Next, we derive a gPC-SG scheme for the governing equation system. To this end, the polynomial approximation of η , q , h_s , z_b and q_s , ψ are written as follows

$$\eta(x, t, \xi) = \sum_{k=0}^{M-1} \hat{\eta}_k(x, t) \Phi_k(\xi), \quad q(x, t, \xi) = \sum_{k=0}^{M-1} \hat{q}_k(x, t) \Phi_k(\xi) \quad (24a, b)$$

$$h_s(x, t, \xi) = \sum_{k=0}^{M-1} \hat{h}_{sk}(x, t) \Phi_k(\xi), \quad z_b(x, t, \xi) = \sum_{k=0}^{M-1} \hat{z}_{bk}(x, t) \Phi_k(\xi) \quad (24c, d)$$

$$q_s(x, t, \xi) = \sum_{k=0}^{M-1} \hat{q}_{sk}(x, t) \Phi_k(\xi), \quad \text{and} \quad \psi(x, t, \xi) = \sum_{k=0}^{M-1} \hat{\psi}_k(x, t) \Phi_k(\xi) \quad (24e, f)$$

Substituting Eq. (24) into system Eq. (8) and bed deformation equation Eq. (3) and then conducting a stochastic Galerkin projection yield the following equations for the gPC coefficients.

$$\frac{\partial \hat{\mathbf{U}}_k}{\partial t} + \frac{\partial \mathbf{F}^I(\hat{\mathbf{U}}_k)}{\partial x} = 0 \quad (25a)$$

$$\frac{\partial \hat{\mathbf{U}}_k}{\partial t} + \frac{\partial \mathbf{F}^{II}(\hat{\mathbf{U}}_k)}{\partial x} = \hat{\mathbf{S}}_{bk} + \hat{\mathbf{S}}_{fk} \quad (25b)$$

in which

$$\hat{\mathbf{U}}_k = \begin{bmatrix} \hat{\eta}_k \\ \hat{q}_k \\ \hat{h}_{s,k} \end{bmatrix}, \quad \mathbf{F}^I = \begin{bmatrix} \hat{q}_k \\ a^2 \hat{\eta}_k \\ \hat{q}_{s,k} \end{bmatrix}, \quad \mathbf{F}^{II} = \begin{bmatrix} 0 \\ \hat{\psi}_k + \frac{1}{2} g \sum_{j,l=0}^{M-1} (\hat{\eta}_j \hat{\eta}_l - 2 \hat{\eta}_j \hat{z}_{b,l}) S_{kjl} - a^2 \hat{\eta}_k \\ 0 \end{bmatrix} \quad (25c, 25d, 25e)$$

$$\hat{\mathbf{S}}_{b,k} = \begin{pmatrix} 0 \\ -g \sum_{j,l=0}^{M-1} \hat{\eta}_j \frac{\partial \hat{z}_{b,l}}{\partial x} S_{kjl} \\ 0 \end{pmatrix} \quad (25f)$$

and

$$\hat{\mathbf{S}}_{f,k} = \begin{pmatrix} 0 \\ \int N(\mathbf{U}) \Phi_k(\xi) \mu(\xi) d\xi \\ \int (E - D) \Phi_k(\xi) \mu(\xi) d\xi \end{pmatrix} \quad (25g)$$

$$\frac{\partial \hat{z}_{b,k}}{\partial t} = - \int \frac{(E-D)}{1-p} \Phi_k(\xi) \mu(\xi) d\xi \quad (26)$$

Subsystems Eqs. (25a and 25b) and the bed deformation equation Eq. (26) are solved using the numerical algorithm described in Section 2.4. The coefficient $\hat{q}_{s,k}$ in Eq. (25d) is computed by applying the gPC-SG approximation to the relation $q_s(\eta - z_b) = h_s q$, giving

$$\sum_{j,l=0}^{M-1} \hat{q}_{s,j} (\hat{\eta}_l - \hat{z}_{b,l}) S_{kjl} = \sum_{j,l=0}^{M-1} \hat{h}_{s,j} \hat{q}_l S_{kjl}, \quad k = 0, \dots, M-1 \quad (27)$$

where $\hat{q}_{s,k}$ is obtained by solving the linear system Eq. (27) once values for \hat{q}_k , $\hat{h}_{s,k}$, $\hat{\eta}_k$ and $\hat{z}_{b,k}$ are available. The coefficient $\hat{\psi}_k$ in Eq. (25e) is determined using the same procedure, applying the relation $\psi(\eta - z_b) = q^2$.

Eq. (25g) involves ensemble averages of the source terms $\int N(\mathbf{U}) \Phi_k(\xi) \mu(\xi) d\xi$ and $\int (E-D) \Phi_k(\xi) \mu(\xi) d\xi$, whereas Eq. (26) includes $\int \frac{(E-D)}{1-p} \Phi_k(\xi) \mu(\xi) d\xi$. These terms are nonlinear and cannot be calculated directly. Instead, these integrals are approximated by Gauss quadrature. When $d = 1$, taking $\int N(\mathbf{U}) \Phi_k(\xi) \mu(\xi) d\xi$ as an example, then

$$\int N(\mathbf{U}) \Phi_k(\xi) \mu(\xi) d\xi \approx \sum_{p=1}^M w_p N \left(\sum_{k=0}^{M-1} \hat{\mathbf{U}}_k \Phi_k(\xi_p) \right) \Phi_k(\xi_p) \mu(\xi_p) \quad (28)$$

where w_p are the quadrature weights and ξ_p are the quadrature points.

3.3. Well-balanced property

Next, we prove that the resulting stochastic SHSM model also satisfies the well-balanced property for a motionless steady state problem with uncertain topography. In the stochastic

setting, it is assumed that the mean free-surface elevation is constant ($\eta \equiv \eta_0$) and the mean discharge is zero ($q \equiv 0$), whilst the bed elevation can have any spatial profile. Therefore, one has $\hat{\eta}_k \equiv \eta_{0,k}$, $\hat{q}_k \equiv 0$, $\hat{\psi}_k \equiv 0$ for all $k = 0, \dots, M-1$. It is straightforward to obtain the values of inter-cell variables after the reconstruction in Step 1:

$$\hat{\eta}_{i-1/2, k}^R = \hat{\eta}_{i+1/2, k}^L = \hat{\eta}_{i+1/2, k}^R = \hat{\eta}_{i+3/2, k}^L = \eta_{0k} \quad (29a)$$

$$\hat{q}_{i-1/2, k}^R = \hat{q}_{i+1/2, k}^L = \hat{q}_{i+1/2, k}^R = \hat{q}_{i+3/2, k}^L = 0 \quad (29b)$$

$$\hat{\psi}_{i-1/2, k}^R = \hat{\psi}_{i+1/2, k}^L = \hat{\psi}_{i+1/2, k}^R = \hat{\psi}_{i+3/2, k}^L = 0 \quad (29c)$$

Then, the second evolution of the variables at the inter-cell $i+1/2$ is conducted following Step 2, from which $\hat{\eta}_{i+1/2, k}^{*L} = \hat{\eta}_{i+1/2, k}^{*R} = \eta_{0k}$, $\bar{\hat{\eta}}_{i+1/2, k}^L = \bar{\hat{\eta}}_{i+1/2, k}^R = \eta_{0k}$, and also

$$\begin{aligned} \bar{\hat{q}}_{i+1/2, k}^L = 0 - \frac{\Delta t}{2\Delta x} & \left[\frac{1}{2} g \sum_{j,l=0}^{M-1} (\hat{\eta}_{0,j} \hat{\eta}_{0,l} - 2\hat{\eta}_{0,j} \hat{z}_{b,i+1/2,l}) S_{kjl} - \frac{1}{2} g \sum_{j,l=0}^{M-1} (\hat{\eta}_{0,j} \hat{\eta}_{0,l} - 2\hat{\eta}_{0,j} \hat{z}_{b,i-1/2,l}) S_{kjl} \right] \\ & + \frac{\Delta t}{2} \left[-g \sum_{j,l=0}^{M-1} (\hat{\eta}_{0,j} \frac{\hat{z}_{b,i+1/2,l} - \hat{z}_{b,i-1/2,l}}{\Delta x}) S_{kjl} \right] = 0 \end{aligned} \quad (30a)$$

$$\begin{aligned} \bar{\hat{q}}_{i+1/2, k}^R = 0 - \frac{\Delta t}{2\Delta x} & \left[\frac{1}{2} g \sum_{j,l=0}^{M-1} (\hat{\eta}_{0,j} \hat{\eta}_{0,l} - 2\hat{\eta}_{0,j} \hat{z}_{b,i+3/2,l}) S_{kjl} - \frac{1}{2} g \sum_{j,l=0}^{M-1} (\hat{\eta}_{0,j} \hat{\eta}_{0,l} - 2\hat{\eta}_{0,j} \hat{z}_{b,i+1/2,l}) S_{kjl} \right] \\ & + \frac{\Delta t}{2} \left(-g \sum_{j,l=0}^M (\hat{\eta}_{0,j} \frac{\hat{z}_{b,i+3/2,l} - \hat{z}_{b,i+1/2,l}}{\Delta x}) S_{kjl} \right) = 0 \end{aligned} \quad (30b)$$

Therefore, the first two components of the flux at inter-cell $i+1/2$ are calculated as

$$\mathbf{F}_{i+1/2}^{I, LF} = \mathbf{F}_{i+1/2}^{I, LW} = \begin{pmatrix} 0 \\ a^2 \hat{\eta}_{0,k} \end{pmatrix} \quad (31a)$$

$$\mathbf{F}_{i+1/2}^{II, LF} = \mathbf{F}_{i+1/2}^{II, LW} = \begin{pmatrix} 0 \\ \frac{1}{2} g \sum_{j,l=0}^{M-1} (\hat{\eta}_{0,j} \hat{\eta}_{0,l} - 2\hat{\eta}_{0,j} \hat{z}_{b,i+1/2,l}) S_{kjl} - a^2 \hat{\eta}_{0,k} \end{pmatrix} \quad (31b)$$

For the inter-cell $i-1/2$, following the above analysis, the first two components of its flux are obtained in a similar way as Eqs. (31a and b), i.e.,

$$\mathbf{F}_{i-1/2}^{I,LF} = \mathbf{F}_{i-1/2}^{I,LW} = \begin{pmatrix} 0 \\ a^2 \hat{\eta}_{0,k} \end{pmatrix} \quad (32a)$$

$$\mathbf{F}_{i-1/2}^{II,LF} = \mathbf{F}_{i-1/2}^{II,LW} = \begin{pmatrix} 0 \\ \frac{1}{2} g \sum_{j,l=0}^{M-1} (\hat{\eta}_{0,j} \hat{\eta}_{0,l} - 2 \hat{\eta}_{0,j} \hat{z}_{b,i-1/2,l}) S_{kjl} - a^2 \hat{\eta}_{0,k} \end{pmatrix} \quad (32b)$$

After the flux computation, the values of $\hat{\eta}_k$ and \hat{q}_k at the next time step are updated to be $\hat{\eta}_k^{n+1} = \hat{\eta}_{0,k}$ and $\hat{q}_k^{n+1} = 0$, and thus a steady static state is exactly preserved at the discrete level, i.e., the well-balanced property is maintained.

4. Test cases

The present stochastic SHSM model is tested against probabilistic numerical case studies, designed to match idealized test of dam break flow over a fixed bed [39] (test case 1) and established laboratory experiments concerning flow-sediment-bed evolutions induced by a sudden dam break [14] (test case 2), and a landslide dam failure [41] (test case 3). As this work is limited to one-dimensional random uncertainty (i.e., $d = 1$), the impact of different single source of uncertainty is individually examined as per test case. A fixed uniform mesh is adopted, and the spatial step is sufficiently fine to ensure mesh independence of the solution, i.e., essentially equivalent solutions are obtained with an even finer mesh. The spatial step Δx is set to be 0.01 m and the Courant number Cr is 0.4. Bed porosity $p = 0.4$ is adopted for all the test cases. The stochastic model is configured with degree $N = 8$ (the highest degree in gPC expansion), resulting in 9 stochastic modes and a probabilistic solution with 9 model realisations. It is also assumed the random variable ξ follows a uniform distribution $\xi \in [-1, 1]$, and so Legendre polynomials are used as the gPC basis. The mean and standard

deviation of the computed results \mathbf{U} are determined as

$$\mu(\mathbf{U}) = \hat{\mathbf{U}}_0 \quad \text{and} \quad \sigma(\mathbf{U}) = \sqrt{\sum_{k=1}^{M-1} \hat{\mathbf{U}}_k^2} \quad (33a, b)$$

4.1. Idealized dam break flow over an uncertain fixed bed (test case 1)

The first test concerns a dam break flow over a fixed bed with perturbation, which is numerically designed by Chertock et al. [39]. The computational domain is $[-1 \text{ m}, 1 \text{ m}]$, and the uncertain bed profile includes a hump centred at $x = 0 \text{ m}$, which is defined as

$$z_b(x, \xi) = \begin{cases} 0.125(\cos(5\pi x) + 1) + 0.1 + 0.1\xi & -0.2 \leq x \leq 0.2 \\ 0.1 + 0.1\xi & \text{otherwise} \end{cases} \quad (34)$$

where $\xi \in [-1, 1]$. Following Chertock et al. [39], the gravitational constant $g = 1$ and the initial water surface is set as

$$\eta(x)_{t=0} = \begin{cases} 1.0 & x \leq 0.0 \\ 0.5 & x > 0.0 \end{cases} \quad (35)$$

At the upstream ($x = -1 \text{ m}$) and downstream ($x = 1 \text{ m}$) boundaries, a transmissive condition [20] was imposed with the values of all the primitive variables at the outlet nodes set equal to those at internal nodes closest to the boundary.

Fig. 1 displays the computed results of the mean and standard deviation of water surface (a1-a2) and discharge (b1 and b2) under uncertain bottom topography at $t = 0.8 \text{ s}$, which show good agreements with the model predictions by Chertock et al. [39]. The standard deviation of water surface $\sigma(\eta)$ presents two major peaks with one located at the wave front and the other around the downstream side of the hump, whereas the standard deviation

of discharge $\sigma(\eta)$ exhibit one peak at the wave front.

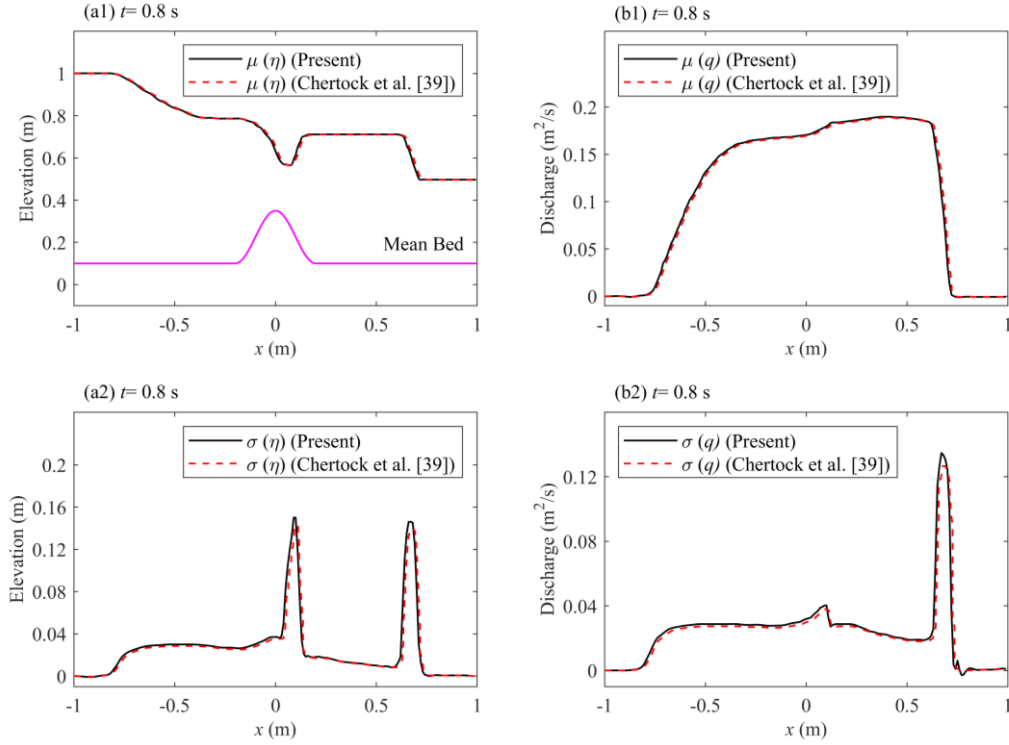


Fig.1. Idealized dam break over a fixed bed with uncertainty: model predictions (dashed lines) by Chertock et al. [31] and present model predictions (solid lines) of mean and standard deviations of water surface and discharge at $t = 0.8$ s.

4.2. Flow-sediment-bed evolution due to instant dam break (test case 2)

This test concerns flow-sediment-bed evolution due to an abrupt, full dam break, for which experiments were previously carried out in a glass-walled flume of dimensions 6 m length \times 0.25 m width \times 0.7 m height by Spinewine [14]. In the experiments, the dam break was created by the rapid downward removal of a thin gate, representing an idealized dam, located at the mid-section of the flume. Initially, the bed was horizontal, composed of non-cohesive sediment saturated with water, and extended both sides of the gate. Here, we

consider one of Spinewine's experiments, where the initial water depth was $h_0 = 35$ cm upstream of the dam, and the bed was dry downstream of the dam. The bed material comprised PVC pellets of diameter 3.92 mm and the density 1580 kg/m³. Numerical modelling was performed until the forward and backward propagating waves reached the downstream and upstream boundaries; thus, the boundary conditions were merely kept at the initial static state.

This test is brought into a probabilistic setting by separately specifying uncertainty in the Manning roughness parameter n and the modification coefficient ϕ for calculating sediment transport rate at capacity regime q_b (see Eq. 7(b)). In general, Manning roughness parameter n in mathematical models of shallow water flows, whether determined through a calibration procedure based on field or laboratory measurements, or obtained from tables of commonly used values, are subject to a high level of uncertainty [47-48]. Likewise, the modification coefficient ϕ is usually calibrated using measured data, which also bears considerable uncertainty. Due to large uncertainties associated with the Manning roughness parameter and the modification coefficient, their range of variability is quite wide. Therefore, both parameters are assumed to have 50% uncertainty. The Manning roughness parameter has a mean value of $n = 0.026 \text{ m}^{-1/3} \text{ s}$ [49], and the mean value of modification ϕ is determined through calibration tests to be 3.0 [17], respectively leading to $n(\xi) = 0.026 + 0.013\xi \text{ (m}^{-1/3} \text{ s)}$, and $\phi(\xi) = 3.0 + 1.5\xi$, where $\xi \in [-1, 1]$.

Figs. 2 and 3 respectively show the probabilistic predictions of water surface and bed profiles for random Manning roughness parameter $n(\xi)$ and modification coefficient $\phi(\xi)$. Corresponding measurements obtained from Spinewine [14] are included. As can be seen, the

measured bed elevations lie within the range of the probabilistic prediction, whereas some discrepancies can be identified between measured and predicted water level profiles. Moreover, the uncertainties in the water level and bed elevation reach peak close to the ‘dam’ and then gradually decrease further downstream. The computed water surface and bed deformation profiles are both sensitive to Manning roughness parameter (see Fig. 2). By contrast, the bed deformation profile is appreciably more sensitive to the modification coefficient ϕ than the water surface profile (as evident in Fig. 3). This difference in behaviour arises because the Manning roughness parameter is embedded directly in the relationships both for resistance (Eq. (4)) and sediment entrainment (Eqs. 7(a, b)). However, the modification coefficient ϕ only appears explicitly in the relationship for sediment entrainment, and thus it only implicitly affects water surface through bed deformation.

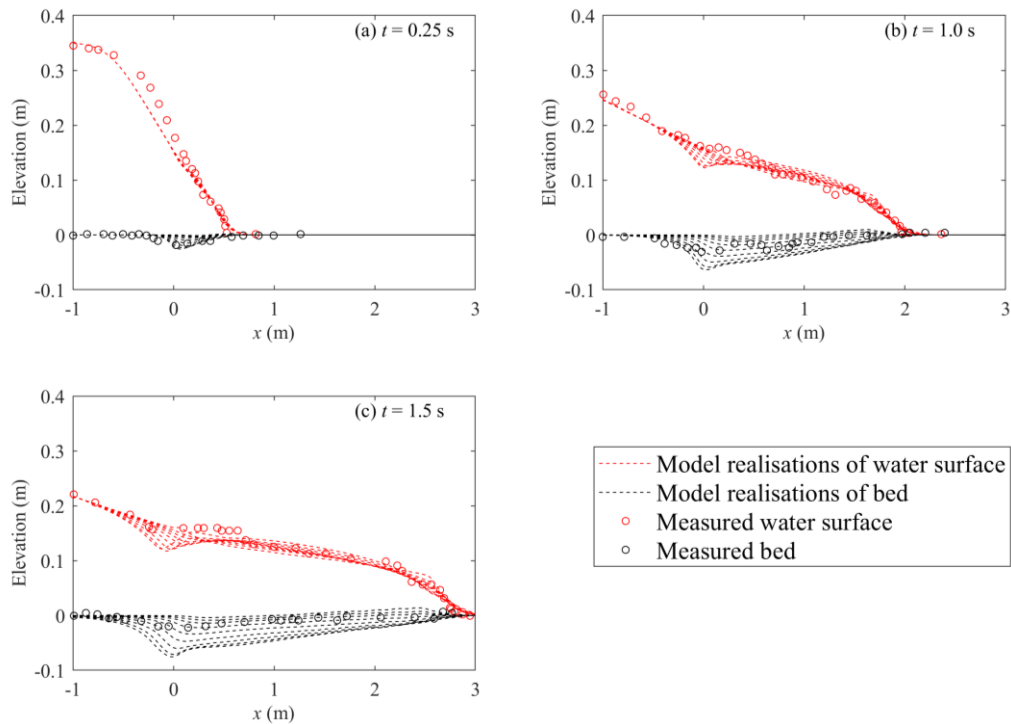


Fig. 2. Sudden dam break over an erodible bed: measurements (open circles) by Spinewine

[14] and probabilistic predictions of water surface and bed profiles (dashed lines) obtained for random Manning roughness parameter $n(\xi)$.

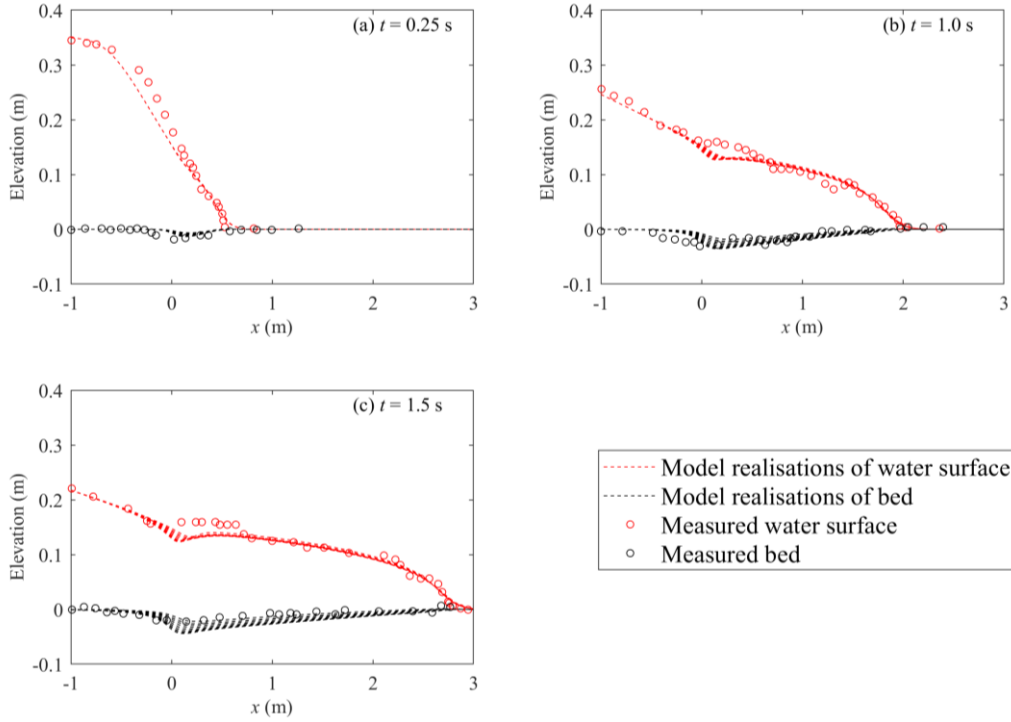


Fig. 3. Sudden dam break over an erodible bed: measurements (open circles) by Spinewine [14] and probabilistic predictions of water surface and bed profiles (dashed lines) obtained for random modification coefficient $\phi(\xi)$.

Fig. 4 shows the spatial-temporal evolution of the standard deviations of water surface, bed elevation, flow velocity, and sediment concentration for random Manning roughness parameter $n(\xi)$ and modification coefficient $\phi(\xi)$. Table 1 summarize the maximum values of the standard deviations of these physical variables. Although both input parameters are perturbed to the same degree of uncertainty (50%), Manning roughness uncertainty has greater impact on the resulting standard deviation surfaces than modification coefficient

uncertainty. In general, output uncertainty in the water surface and bed elevation due to input uncertainty in the Manning roughness and modification coefficient both accumulates and extends downstream as the dam-break wave propagates with time. Furthermore, the standard deviations of water surface $\sigma(\eta)$ and bed elevation $\sigma(z_b)$ peak close to the ‘dam’ site and then gradually decrease in the stream-wise direction. Unlike $\sigma(\eta)$ and $\sigma(z_b)$, the standard deviation of flow velocity $\sigma(u)$ exhibits a peak near the wave front, and the standard deviation of sediment concentration $\sigma(c)$ presents a double-peaked behaviour with one peak located at the wave front and the other approximately at the centre of wave. A similar multi-peaked structure in the standard deviation of concentration has also been observed for advection-diffusion in random media [27].

Table 1 Summary of maximum standard deviations of all the physical variables (Test case 1)

Results	Source of uncertainty	
	Manning roughness $n(\xi)$	Modification coefficient $\phi(\xi)$
$\sigma(\eta)$ (m)	0.023	0.010
$\sigma(z_b)$ (m)	0.041	0.014
$\sigma(u)$ (m/s)	0.462	0.108
$\sigma(c)$	0.289	0.083

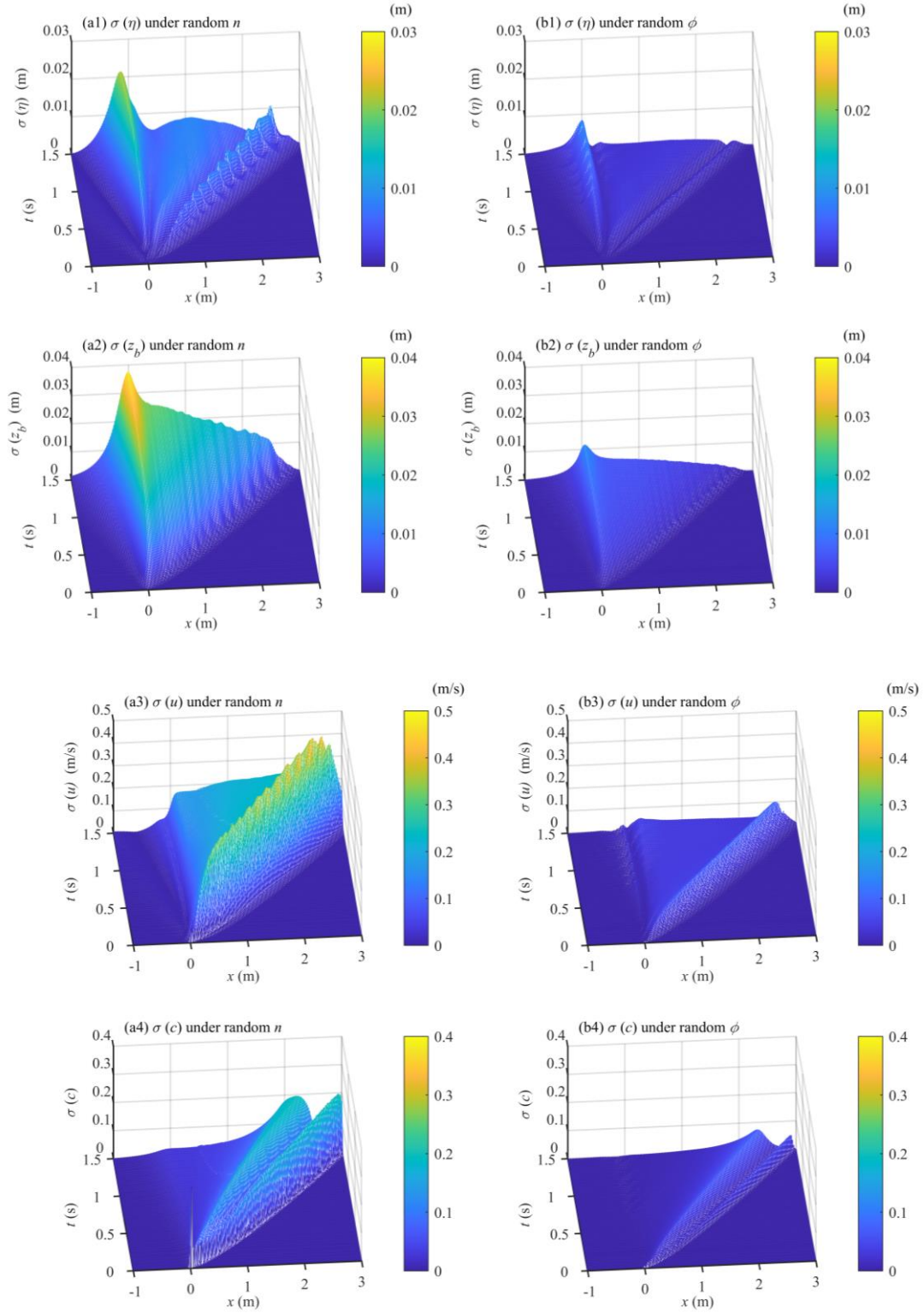


Fig. 4. Spatial-temporal evolution of standard deviations of water surface, bed elevation, flow velocity, and sediment concentration for random (a1-a4) Manning roughness parameter $n(\xi)$ and (b1-b4) modification coefficient $\phi(\xi)$.

4.3. Flow-sediment-bed evolution due to landslide dam failure (test case 3)

We now examine flow-sediment-bed evolution due to landslide dam failure, and compare model predictions with measured data obtained from one of a series of flume experiments carried out by Cao et al. [41]. The experiments were undertaken in a flume of dimensions 80 m length \times 1.2 m width \times 0.8 m height (Fig. 5), bed slope of 0.001, and Manning's bed roughness coefficient $n = 0.012 \text{ m}^{-1/3} \text{ s}$. Twelve automatic water-level probes measured the stage time histories at different locations along the centre line of the flume. In the experiments, dam failure occurred through erosion caused by overtopping flow. Once dam failure commenced, flow upstream of the dam receded quickly. By contrast, the downstream flow underwent three stages: initial rising, subsequent gradual recession, and final stabilization. For further details, please see Cao et al. [41]. The present case of interest concerns a landslide dam comprising uniform sediment with no initial breach (i.e., F- Case 11 considered by Cao et al.'s paper). In this case, the initial upstream and downstream slopes of the dam were 1/2 and 1/3. The inlet flow discharge was $0.042 \text{ m}^3/\text{s}$. Initial static water depths immediately upstream and downstream of the dam were 0.054 m and 0.048 m. At the outlet of the flume, a 0.15 m-high weir controlled the downstream water level so that it remained at the initial depth. The dam comprised non-cohesive sediment of median diameter 0.8 mm and specific gravity 1.65. At the inlet boundary of numerical model, the flow discharge was specified, and the water depth and velocity determined by the method of characteristics. Observations during the course of the experiments had shown that a hydraulic drop occurred downstream of the weir, so the outflow did not affect flow upstream of the weir. Hence, a

transmissive condition [20] was imposed at the downstream boundary (80 m).

In addition to the Manning roughness and the modification coefficient, we also investigated the impact of uncertainty in the inflow discharge, which is subject to considerable uncertainty due to measurement error [48]. Specifically, the steady inflow discharge is assumed to have 15% uncertainty, which is a suitable range for fluvial flow modelling [48]. Similar to test case 2, the Manning roughness parameter and the modification coefficient are both perturbed by 50% uncertainty. Hence, $q_{in}(\xi) = 0.042 + 0.0063\xi$ (m³/s), $n(\xi) = 0.012 + 0.006\xi$ (m^{-1/3}s), and $\phi(\xi) = 6.0 + 3.0\xi$, where $\xi \in [-1, 1]$.

Figs. 6, 7 and 8 respectively show the probabilistic stage time histories predicted by the stochastic SHSM model for random inflow discharge $q_{in}(\xi)$, Manning roughness parameter $n(\xi)$, and modification coefficient $\phi(\xi)$. Corresponding measurements obtained by Cao et al. [41] at selected locations along the channel are superimposed. Stations CS 1, CS 5, CS 8 and CS 12 are located 19 m, 40 m, 54 m and 73.5 m downstream of the inlet (Fig. 5). CS 1 and CS 5 are upstream of the dam, whereas CS 8 and CS 12 are downstream. The model predictions comprise 9 model realisations as plotted individually. Figs. 6, 7, and 8 collectively show that the new model satisfactorily reproduces the stage time histories, in that the probabilistic predictions bounds all the measured data. Moreover, it is demonstrated that the computed results are most sensitive to inflow discharge q_{in} , followed by Manning roughness parameter n , and then modification coefficient ϕ . Model sensitivity to uncertainty in n and ϕ is considerably constrained compared to uncertainty in q_{in} . This is confirmed by the output uncertainties in response to perturbed n and ϕ (by 50%), which are considerably smaller than their counterpart for perturbed q_{in} (by 15%).

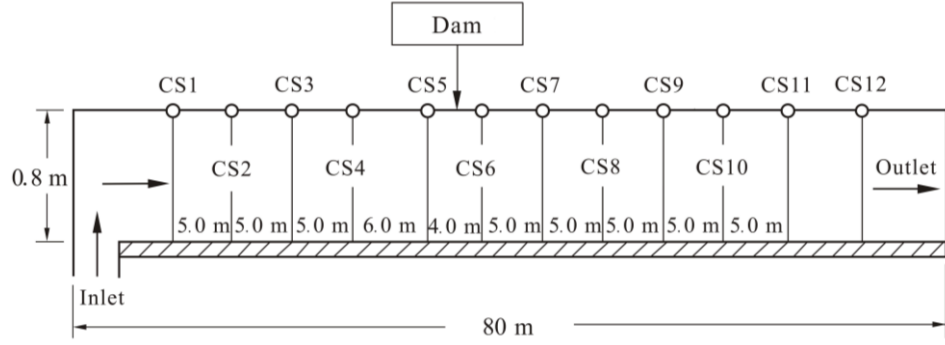


Fig. 5. Cao et al.'s [41] experimental setup for landslide dam failure [figure adapted from Li et al. [17]].

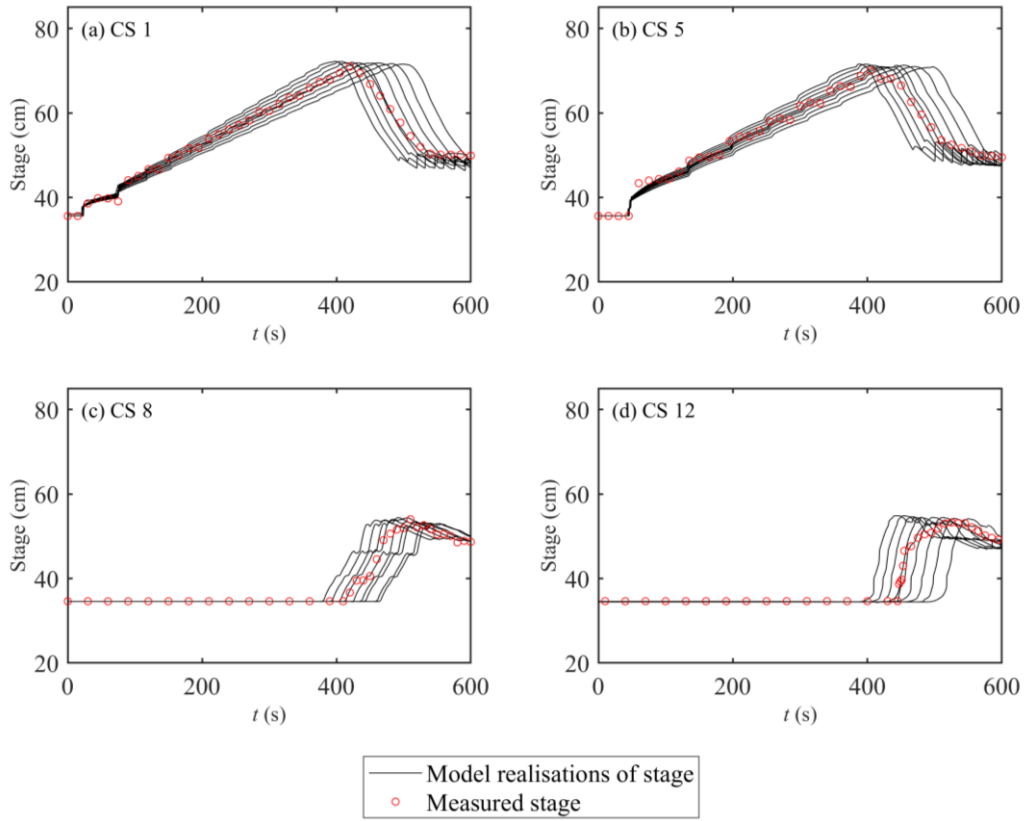


Fig. 6. Landslide dam failure: measurements (open circles) for F-Case 11 by Cao et al. [41] and probabilistic predictions (solid lines) of stage time histories at 4 gauge points along the flume for random inflow discharge $q_{in}(\xi)$.

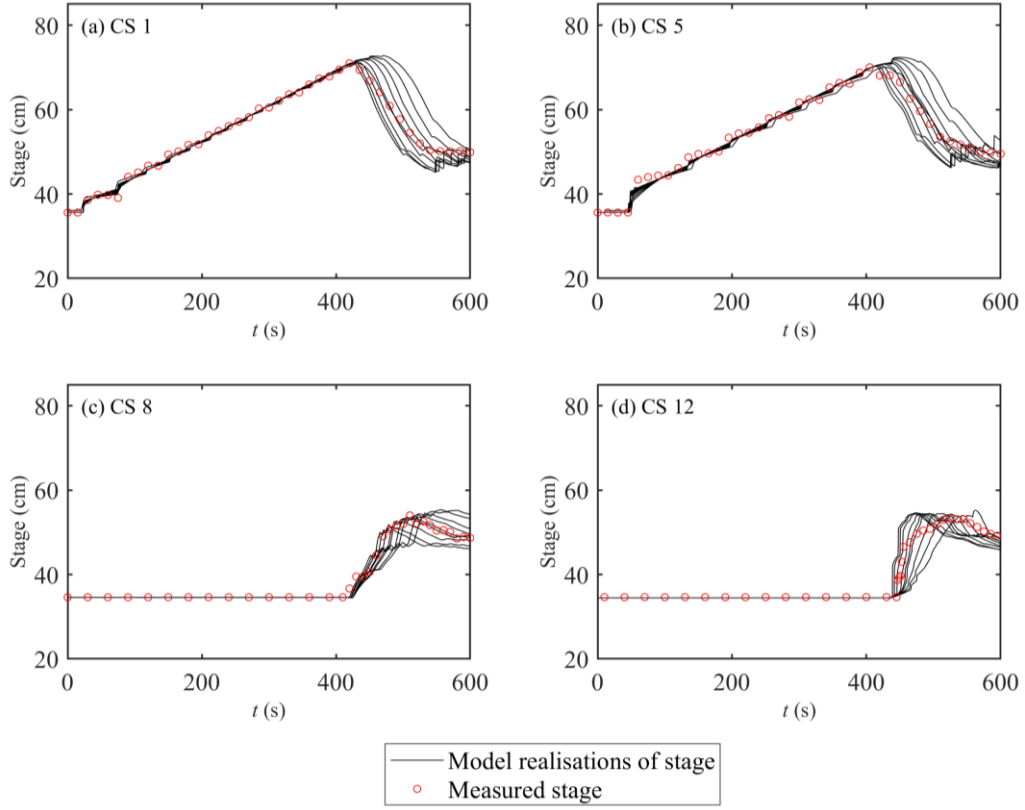


Fig. 7. Landslide dam failure: measurements (open circles) for F-Case 11 by Cao et al. [41] and probabilistic predictions (solid lines) of stage time histories at 4 gauge points along the flume for random Manning's coefficient $n(\xi)$.

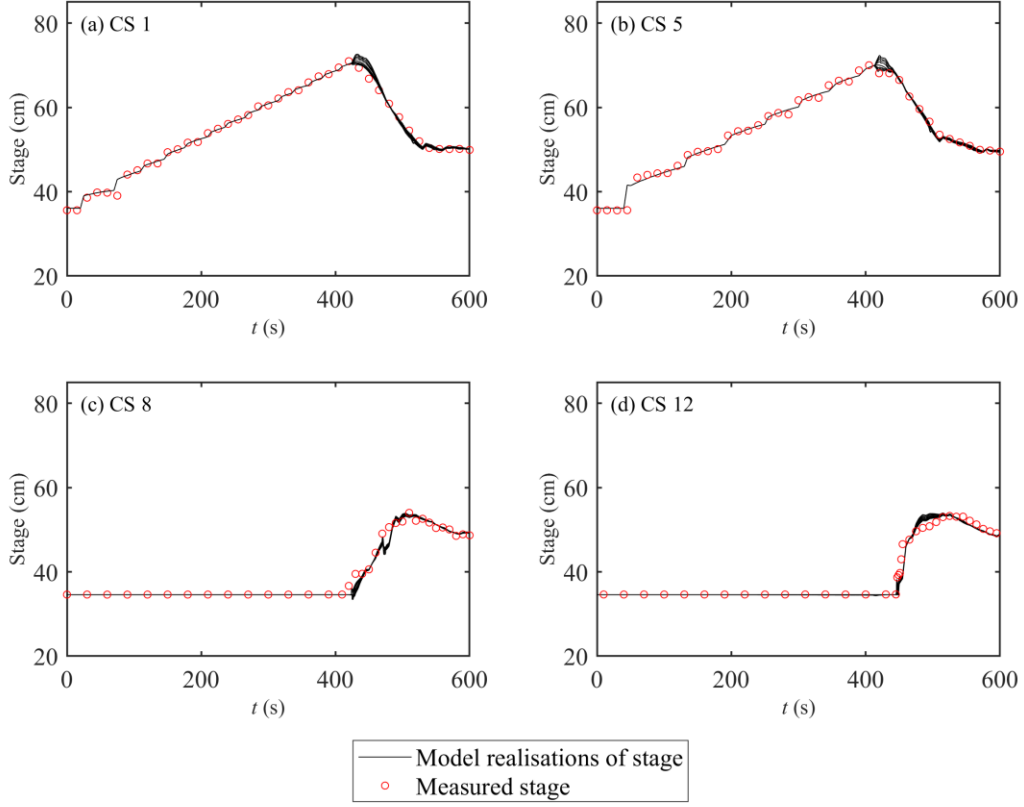


Fig. 8. Landslide dam failure: measurements (open circles) for F-Case 11 by Cao et al. [41] and probabilistic predictions (solid lines) of stage time histories at 4 gauge points along the flume for random modification coefficient $\phi(\xi)$.

Figs. 9 and 10 respectively present the probabilistic predictions of water surface and bed profiles for random inflow discharge and Manning roughness parameter, with measured data from Cao et al. [41] for water surface superimposed. Echoing Figs. 6 and 7, the computed results are generally more sensitive to uncertainty in inflow discharge than in Manning roughness parameter. Compared to bed deformation, the water surface profile is more sensitive to the input perturbations. The output uncertainty in water surface is relatively large along the channel for random $q_{in}(\xi)$ because the uncertainty in inflow discharge enters from the upstream boundary and propagates downstream (Fig. 9a). The output uncertainty in

the water surface for random $n(\xi)$ only develops after the onset of dam failure (Fig. 10a). At $t = 430$ s, the overtopping flow erodes the downstream surface of the dam, causing the formation of a hydraulic drop and a hydraulic jump near the dam site. Further erosion is evident by $t = 450$ s, with two hydraulic jumps occurring downstream of the dam. The uncertainties in the water surface and bed elevation for random inflow discharge (Fig. 9b and 9c) and Manning roughness (Fig. 10b and 10c) exhibit appreciable increase close to the hydraulic drop and jump. After $t > 600$ s, the free surface of the flow is nearly horizontal, unable further to erode the dam, and the dam failure process essentially terminates. At this stage, the output uncertainties in the water surface and bed elevation due to inflow discharge perturbation revert almost to zero (Fig. 9d), whereas those under random Manning roughness parameter still persist, despite their magnitude decreasing significantly (Fig. 10d).

Fig. 11 shows the spatial-temporal evolution of the standard deviations of water surface, bed elevation, flow velocity and sediment concentration for random inflow discharge $q_{in}(\xi)$ and Manning roughness parameter $n(\xi)$. Table 2 list the maximum standard deviations of these physical variables. Fig. 11 and Table 2 collectively confirms that inflow discharge uncertainty has greater impact on the resulting standard deviation than Manning roughness uncertainty. Before the water flows over the top of the dam, the standard deviations of water surface $\sigma(\eta)$ and flow velocity $\sigma(u)$ only increase upstream of the dam site, and the standard deviation of the bed elevation $\sigma(z_b)$ and sediment concentration $\sigma(c)$ remain zero. After the dam is overtopped and the dam breach commences, the standard deviations of all the physical variables increase rapidly with time and extend toward the outlet. As the dam failure process decreases and finally comes to a halt, the standard deviations also gradually

shrink.

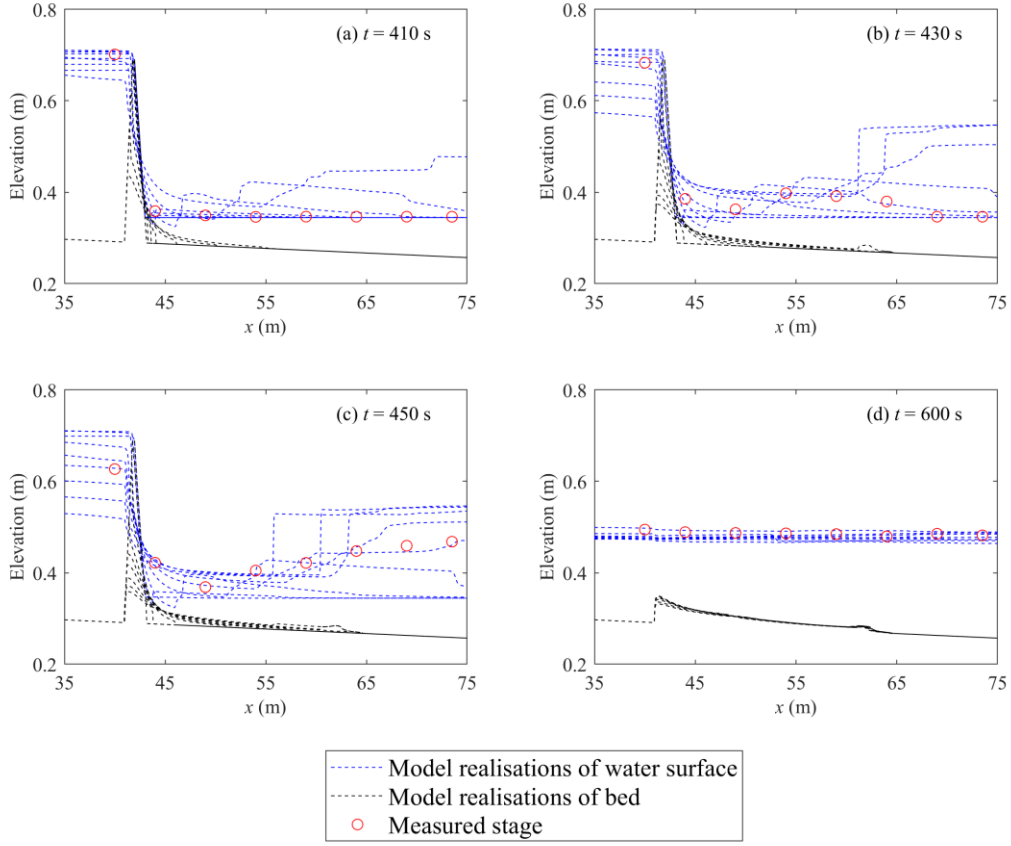


Fig. 9. Landslide dam failure: measured water surface (open circles) for F-Case 11 by Cao et al. [41] and probabilistic predictions of water surface, and bed profiles (dashed lines) along a channel for random inflow discharge $q_{in}(\xi)$.

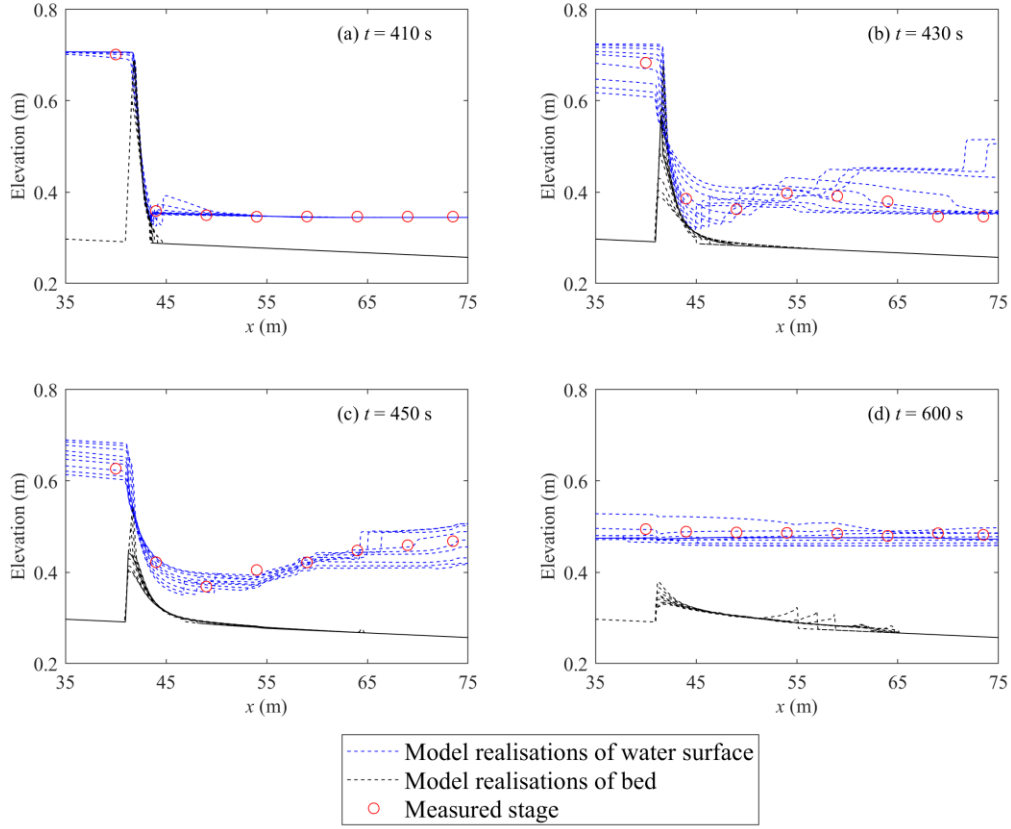


Fig. 10. Landslide dam failure: measured water surface (open circles) for F-Case 11 by Cao et al. [41] and model realisations of water surface, and bed profiles (dashed lines) along a channel for random Manning's coefficient $n(\xi)$.

Table 2 Summary of maximum standard deviations of all the physical variables (test case 3)

Results	Source of uncertainty	
	Inflow discharge $q_{in}(\xi)$	Manning roughness $n(\xi)$
$\sigma(\eta)$ (m)	0.148	0.068
$\sigma(z_b)$ (m)	0.261	0.118
$\sigma(u)$ (m/s)	1.315	0.924
$\sigma(c)$	0.455	0.423

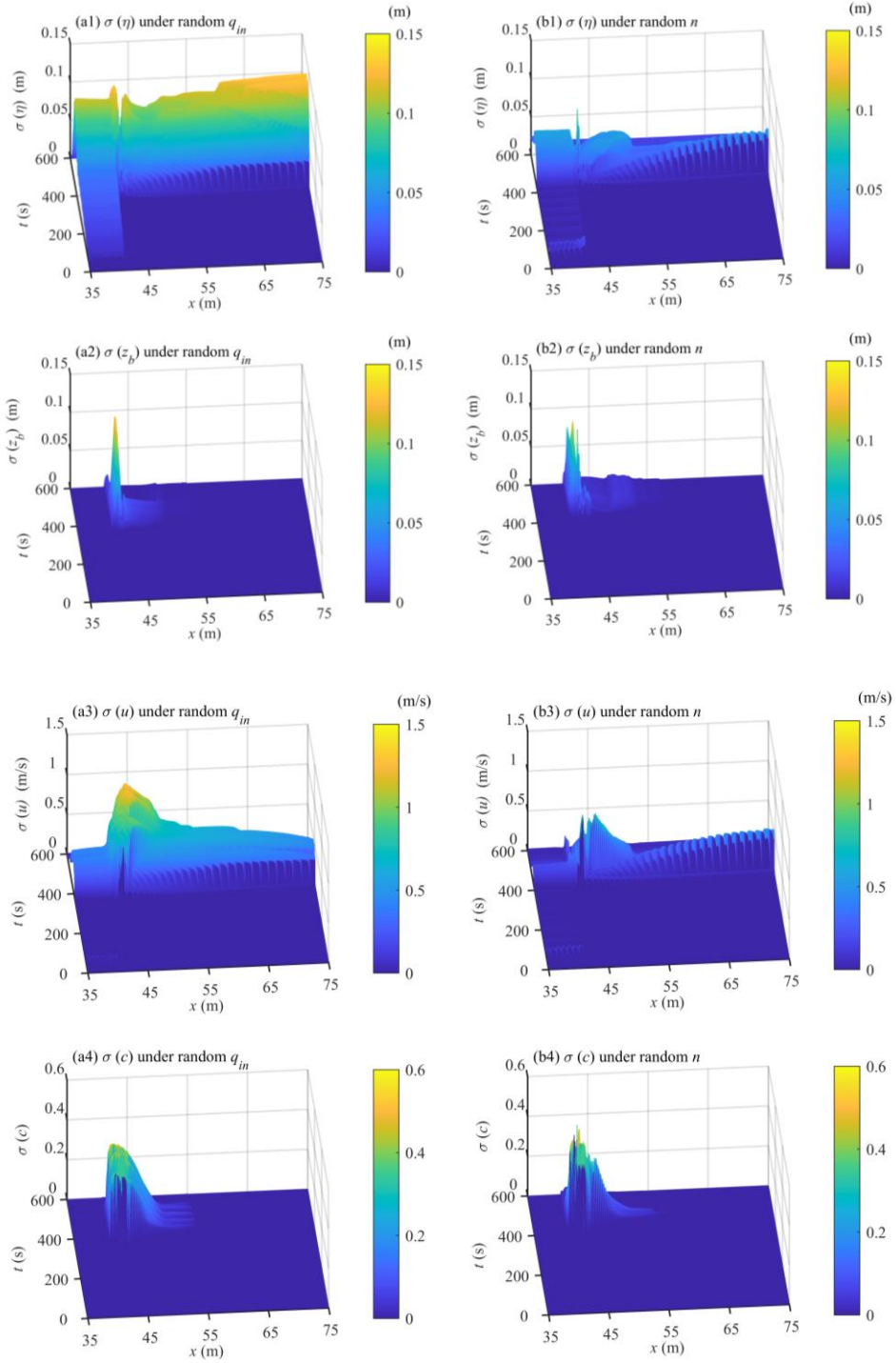


Fig. 11. Landslide dam failure: spatial-temporal evolution of standard deviations of water surface, bed elevation, flow velocity and sediment concentration for random (a1-a4) inflow discharge $q_{in}(\xi)$ and (b1-b4) Manning's coefficient $n(\xi)$.

5. Conclusions

A new stochastic SHSM model based on a well-balanced, operator-splitting-based, stochastic Galerkin method is proposed for probabilistic shallow water-sediment flows over erodible beds. Benchmark probabilistic numerical tests verify the model for wave propagation triggered by idealized dam break over a fixed bed and flow-sediment-bed evolution driven by sudden dam break and by landslide dam failure, with uncertainty introduced in initial and boundary conditions. The model captures both possible realization and standard deviation of the solutions, while also simulating strongly nonlinear flow behaviour. Although this study represents a first attempt to model probabilistic shallow water-sediment flows over an erodible bed in a stochastic Galerkin setting, further research is still required to [extend the proposed model to multiple joint uncertainties and also validate the model for](#) flows containing strong discontinuities in random space. It is also essential that a more solid theoretical foundation is established for the present model and that it is extended to two spatial dimensions for application to natural flows. These topics are reserved for future study.

Acknowledgements

This work was funded by the Natural Science Foundation of China under Grant No. 11802211 and the China Postdoctoral Science Foundation under Grant No. 2018M632917.

References

- [1] W. Wu, Computational river dynamics, Taylor and Francis, London, UK, 2007.
- [2] W. Wu, W. Rodi, T. Wenka, 3D numerical modeling of flow and sediment transport in open channels, *J. Hydraul. Eng.* 126(1) (2000) 4-15.
[https://doi.org/10.1061/\(ASCE\)0733-9429\(2000\)126:1\(4\)](https://doi.org/10.1061/(ASCE)0733-9429(2000)126:1(4)).
- [3] H.W. Fang, G.Q. Wang, Three-dimensional mathematical model of suspended-sediment transport, *J. Hydraul. Eng.* 126(8) (2000) 578-592.
[https://doi.org/10.1061/\(ASCE\)0733-9429\(2000\)126:8\(578\)](https://doi.org/10.1061/(ASCE)0733-9429(2000)126:8(578)).
- [4] R. Marsooli, W. Wu, 2015. Three-dimensional numerical modeling of dam-break flows with sediment transport over movable beds. *J. Hydraul. Eng.* 141(1), 04014066.
[https://doi.org/10.1061/\(ASCE\)HY.1943-7900.0000947](https://doi.org/10.1061/(ASCE)HY.1943-7900.0000947).
- [5] T. Takahashi, H. Nakagawa, T. Harada, Y. Yamashiki, Routing debris flows with particle segregation, *J. Hydraul. Eng.* 118(11) (1992) 1490-1507.
[https://doi.org/10.1061/\(ASCE\)0733-9429\(1992\)118:11\(1490\)](https://doi.org/10.1061/(ASCE)0733-9429(1992)118:11(1490)).
- [6] Z. Cao, G. Pender, S. Wallis, P. Carling, Computational dam-break hydraulics over erodible sediment bed, *J. Hydraul. Eng.* 130(7) (2004) 689-703.
[http://doi.org/10.1061/\(ASCE\)0733-9429\(2004\)130:7\(689\)](http://doi.org/10.1061/(ASCE)0733-9429(2004)130:7(689)).
- [7] A. Armanini, L. Fraccarollo, G. Rosatti, Two-dimensional simulation of debris flows in erodible channels, *Comput. Geosci.* 35 (2009) 993-1006.
<https://doi.org/10.1016/j.cageo.2007.11.008>.
- [8] H. Qian, Z. Cao, H. Liu, G. Pender, Numerical modelling of alternate bar formation, development and sediment sorting in straight channels, *Earth Surf. Proc. Land.* 42(4) (2017) 555-574. <https://doi.org/10.1002/esp.3988>.
- [9] H. Qian, Z. Cao, G. Pender, H. Liu, P. Hu, Well-balanced numerical modeling of non-uniform sediment transport in alluvial rivers, *Int. J. Sediment Res.* 30(2) (2015) 117-130.
<http://doi.org/10.1016/j.ijsrc.2015.03.002>.

- [10] P. Hu, Y. Lei, J. Han, Z. Cao, H. Liu, Z. He, Computationally efficient modeling of hydro-sediment-morphodynamic processes using a hybrid local time step/global maximum time step, *Adv. Water Resour.* 127(2019) 26-38.
<https://doi.org/10.1016/j.advwatres.2019.03.006>
- [11] S.P. Pudasaini, 2012. A general two-phase debris flow model, *J. Geophys. Res.* 117, F03010. <https://doi.org/10.1029/2011JF002186>.
- [12] C. Di Cristo, M. Greco, M. Iervolino, A. Leopardi, A. Vacca, 2016. Two-dimensional two-phase depth-integrated model for transients over mobile bed, *J. Hydraul. Eng.* 142(2), 04015043. [http://doi.org/10.1061/\(ASCE\)HY.1943-7900.0001024](http://doi.org/10.1061/(ASCE)HY.1943-7900.0001024).
- [13] J. Li, Z. Cao, K. Hu, G. Pender, Q. Liu, A depth- averaged two- phase model for debris flows over erodible beds. *Earth Surf. Proc. Landf.* 43(4) (2018) 817-839.
<https://doi.org/10.1002/esp.4283>.
- [14] B. Spinewine, Two-layer flow behaviour and the effects of granular dilatancy in dam-break induced sheetflow, PhD thesis, Université Catholique de Louvain, Belgium, 2005.
- [15] E.D. Fernández-Nieto, F. Bouchut, D. Bresch, M.J. Castro Díaz, A. Mangeney, A new Savage-Hutter type model for submarine avalanches and generated tsunami, *J. Comput. Phys.* 27(16) (2008) 7720-7754. <https://doi.org/10.1016/j.jcp.2008.04.039>.
- [16] C. Adduce, G. Sciortino, S. Proietti, Gravity currents produced by lock exchanges: experiments and simulations with a two-layer shallow-water model with entrainment. *J. Hydraul. Eng.* 138(2) (2012) 111-121.
[https://doi.org/10.1061/\(ASCE\)HY.1943-7900.0000484](https://doi.org/10.1061/(ASCE)HY.1943-7900.0000484).
- [17] J. Li, Z. Cao, G. Pender, Q. Liu, A double layer-averaged model for dam-break flows over mobile bed. *J. Hydraul. Res.* 51(5) (2013) 518-534.
<https://doi.org/10.1080/00221686.2013.812047>.
- [18] Z. Cao, J. Li, G. Pender, Q. Liu, 2015. Whole-process modelling of reservoir turbidity currents by a double layer-averaged model. *J. Hydraul. Eng.* 141(2), 04014069. [http://doi.org/10.1061/\(ASCE\)HY.1943-7900.0000951](http://doi.org/10.1061/(ASCE)HY.1943-7900.0000951).

- [19] J. Li, Z. Cao, Y. Cui, A.G.L. Borthwick, Barrier lake formation due to landslide impacting a river: A numerical study using a double layer-averaged two-phase flow model, *Appl. Math. Model.* 80 (2020) 574-601. <https://doi.org/10.1016/j.apm.2019.11.031>
- [20] E.F. Toro, *Shock-capturing methods for free-surface shallow flows*, John Wiley and Sons, Chichester, UK, 2001.
- [21] D. Xiu, Fast numerical methods for stochastic computations: a review, *Commun. Comput. Phys.* 5(2-4) (2009) 242-272. DOI
- [22] R.G. Ghanem, P.D. Spanos, *Stochastic finite elements: a spectral approach*, Springer, New York, 2003.
- [23] D. Xiu, J.S. Hesthaven, High-order collocation methods for differential equations with random inputs, *SIAM J. Sci. Comput.* 27(3) (2005) 1118-1139. <https://doi.org/10.1137/040615201>.
- [24] D. Xiu, *Numerical methods for stochastic computations*, Princeton University Press, Princeton, USA, 2010.
- [25] S. Mishra, C. Schwab, J. Sukys, Multilevel Monte Carlo finite volume methods for shallow water equations with uncertain topography in multi-dimension, *SIAM J. Sci. Comput.* 34(6) (2012) B761-B784. <https://doi.org/10.1137/110857295>.
- [26] H.C. Elman, C.W. Miller, E.T. Phipps, R.S. Tuminaro, Assessment of collocation and Galerkin approaches to linear diffusion equations with random data, *Int. J. Uncertain. Quant.* 1(1) (2011) 19-33. <http://doi.org/10.1615/Int.J.UncertaintyQuantification.v1.i1.20>.
- [27] D. Xiu, J. Shen, Efficient stochastic Galerkin methods for random diffusion equations, *J. Comput. Phys.* 228(2) (2009) 266-281. <https://doi.org/10.1016/j.jcp.2008.09.008>.
- [28] J. Hu, S. Jin, A stochastic Galerkin method for the Boltzmann equation with uncertainty, *J. Comput. Phys.* 315 (2016) 150-168. <https://doi.org/10.1016/j.jcp.2016.03.047>
- [29] R. Shu, J. Hu, S. Jin, A stochastic Galerkin method for the Boltzmann equation with multi-dimensional random inputs using sparse wavelet bases, *Numer. Math-Theory Me.*

10(02) (2017) 465-488. <http://doi.org/10.4208/nmtma.2017.s12>.

[30] S. Jin, R. Shu, A stochastic asymptotic-preserving scheme for a kinetic-fluid model for disperse two-phase flows with uncertainty, *J. Comput. Phys.* 335 (2017) 905-924.

<https://doi.org/10.1016/j.jcp.2017.01.059>.

[31] L. Ge, K.F. Cheung, M.H. Kobayashi, Stochastic solution for uncertainty propagation in nonlinear shallow-water equations, *J. Hydraul. Eng.* 134 (12) (2008) 1732–1743.

[https://doi.org/10.1061/\(ASCE\)0733-9429\(2008\)134:12\(1732\)](https://doi.org/10.1061/(ASCE)0733-9429(2008)134:12(1732)).

[32] J. Shaw, G. Kesserwani, 2020. Stochastic Galerkin finite volume shallow flow model: well-balanced treatment over uncertain topography, *J. Hydraul. Eng.* 146(3), 04020005.

[https://doi.org/10.1061/\(ASCE\)HY.1943-7900.0001705](https://doi.org/10.1061/(ASCE)HY.1943-7900.0001705).

[33] B. Després, G. Poëtte, D. Lucor, Robust uncertainty propagation in systems of conservation laws with the entropy closure method, in: H. Bijl, D. Lucor, S. Mishra, C. Schwab, (Eds.), *Uncertainty Quantification in Computational Fluid Dynamics*, Springer, Berlin, 2013, pp. 105–149.

[34] J. Hu, S. Jin, D. Xiu, A Stochastic Galerkin Method for Hamilton--Jacobi Equations with Uncertainty, *SIAM J. Sci. Comput.* 37(5) (2015) A2246-A2269.

<https://doi.org/10.1137/140990930>.

[35] H. Grad, On the kinetic theory of rarefied gases, *Commun. Pur. Appl. Math.* 2(4) (1949) 331-407.

[36] G. Poëtte, B. Després, D. Lucor, Uncertainty quantification for systems of conservation laws, *J. Comput. Phys.* 228(7) (2009) 2443-2467. <https://doi.org/10.1016/j.jcp.2008.12.018>.

[37] P. Pettersson, G. Iaccarino, J. Nordström, A stochastic Galerkin method for the Euler equations with Roe variable transformation, *J. Comput. Phys.* 257 (2014) 481-500.

<https://doi.org/10.1016/j.jcp.2013.10.011>

[38] A. Chertock, S. Jin, A. Kurganov, An operator splitting based stochastic Galerkin method for the one-dimensional compressible Euler equations with uncertainty.

<http://www.math.wisc.edu/~jin/research.html>, 2015a (accessed 24 December 2020).

- [39] A. Chertock, S. Jin, A. Kurganov, A well-balanced operator splitting based stochastic Galerkin method for the one-dimensional Saint-Venant system with uncertainty. <http://www.math.wisc.edu/~jin/research.html>, 2015b. (accessed 24 December 2020).
- [40] S. Gottlieb, D.I. Ketcheson, C.W. Shu, Strong stability preserving Runge-Kutta and multistep time discretizations, World Scientific, Singapore, 2011.
- [41] Z. Cao, Z. Yue, G. Pender, Landslide dam failure and flood hydraulics. Part I: experimental investigation, *Nat. Hazards* 59(2) (2011) 1003-1019. <http://doi.org/10.1007/s11069-011-9814-8>.
- [42] A. Gorodetsky, Y. Marzouk, Efficient localization of discontinuities in complex computational simulations, *SIAM J. Sci. Comput.* 36(6) (2014) A2584-A2610. <https://doi.org/10.1137/140953137>
- [43] P. Pettersson, A. Doostan, J. Nordstrom, Level set methods for stochastic discontinuity detection in nonlinear problems, *J. Comput. Phys.* 392 (2019) 511-531. <https://doi.org/10.1016/j.jcp.2019.04.053>.
- [44] Y. V. Halder, B. Sanderse, B. Koren, An adaptive minimum spanning tree multielement method for uncertainty quantification of smooth and discontinuous responses, *SIAM J. Sci. Comput.* 41(6) (2019) A3624-A3648. <https://doi.org/10.1137/18M1219643>.
- [45] G.K. Batchelor, An introduction to fluid dynamics, Cambridge University Press, Cambridge, 1967.
- [46] R.J. Zhang, J.H. Xie, Sedimentation research in China-systematic selections, China Water and Power Press, Beijing, 1993.
- [47] M.S. Horritt, A linearized approach to flow resistance uncertainty in a 2-D finite volume model of flood flow, *J. Hydrol.* 316(1-4) (2005) 13-27. <https://doi.org/10.1016/j.jhydrol.2005.04.009>.
- [48] P.D. Bates, F. Pappenberger, R.J. Romanowicz, Uncertainty in Flood Inundation Modelling, in: K.J. Beven, J. Hall (Eds.), Applied uncertainty analysis for flood risk management. Imperial College Press, London, 2014, pp. 232–269.

https://doi.org/10.1142/9781848162716_0010.

[49] Y. Zech, S. Soares-Frazão, B. Spinewine, N. Grelle, Dam-break induced sediment movement: Experimental approaches and numerical modelling, J. Hydraul. Res. 46(2) (2008) 176-190. <https://doi.org/10.1080/00221686.2008.9521854>.

List of figure captions

Fig.1. Idealized dam break over a fixed bed with uncertainty: model predictions (dashed lines) by Chertock et al. [31] and present model predictions (solid lines) of mean and standard deviations of water surface and discharge at $t = 0.8$ s.

Fig. 2. Sudden dam break over an erodible bed: measurements (open circles) by Spinewine [14] and probabilistic predictions of water surface and bed profiles (dashed lines) obtained for random Manning roughness parameter $n(\xi)$.

Fig. 3. Sudden dam break over an erodible bed: measurements (open circles) by Spinewine [14] and probabilistic predictions of water surface and bed profiles (dashed lines) obtained for random modification coefficient $\phi(\xi)$.

Fig. 4. Spatial-temporal evolution of standard deviations of water surface, bed elevation, flow velocity, and sediment concentration for random (a1-a4) Manning roughness parameter $n(\xi)$ and (b1-b4) modification coefficient $\phi(\xi)$.

Fig. 5. Cao et al.'s [41] experimental setup for landslide dam failure [figure adapted from Li et al. [17]].

Fig. 6. Landslide dam failure: measurements (open circles) for F-Case 11 by Cao et al. [41] and probabilistic predictions (solid lines) of stage time histories at 4 gauge points along the flume for random inflow discharge $q_{in}(\xi)$.

Fig. 7. Landslide dam failure: measurements (open circles) for F-Case 11 by Cao et al. [41] and probabilistic predictions (solid lines) of stage time histories at 4 gauge points along the flume for random Manning's coefficient $n(\xi)$.

Fig. 8. Landslide dam failure: measurements (open circles) for F-Case 11 by Cao et al. [41] and probabilistic predictions (solid lines) of stage time histories at 4 gauge points along the flume for random modification coefficient $\phi(\xi)$.

Fig. 9. Landslide dam failure: measured water surface (open circles) for F-Case 11 by Cao et al. [41] and probabilistic predictions of water surface, and bed profiles (dashed lines) along a channel for random inflow discharge $q_{in}(\xi)$.

Fig. 10. Landslide dam failure: measured water surface (open circles) for F-Case 11 by Cao et al. [41] and model realisations of water surface, and bed profiles (dashed lines) along a channel for random Manning's coefficient $n(\xi)$.

Fig. 11. Landslide dam failure: spatial-temporal evolution of standard deviations of water surface, bed elevation, flow velocity and sediment concentration for random (a1-a4) inflow discharge $q_{in}(\xi)$ and (b1-b4) Manning's coefficient $n(\xi)$.

List of tables

Table 1 Summary of maximum standard deviations of all the physical variables (Test case 1)

Results	Source of uncertainty	
	Manning roughness $n(\xi)$	Modification coefficient $\phi(\xi)$
$\sigma(\eta)$ (m)	0.023	0.010
$\sigma(z_b)$ (m)	0.041	0.014
$\sigma(u)$ (m/s)	0.462	0.108
$\sigma(c)$	0.289	0.083

Table 2 Summary of maximum standard deviations of all the physical variables (test case 3)

Results	Source of uncertainty	
	Inflow discharge $q_{in}(\xi)$	Manning roughness $n(\xi)$
$\sigma(\eta)$ (m)	0.148	0.068
$\sigma(z_b)$ (m)	0.261	0.118
$\sigma(u)$ (m/s)	1.315	0.924
$\sigma(c)$	0.455	0.423